Fonoll-Rubio *et al. Energy Mater.* **2025**, *5*, 500122
DOI: 10.20517/energymater.2024.189

Energy Materials

Article

Open Access

Check for updates

Advancing kesterite absorbers with bronze-based precursors through physical deposition routes: a step toward stable and sustainable industrial photovoltaic technology

Robert Fonoll-Rubio[1], Jesús Roberto González-Castillo[2], Jacob Andrade-Arvizu[1], Xavier Alcobé[3], Alejandro Pérez-Rodríguez[1,4], Pedro Vidal-Fuentes[1], Maxim Guc[1,*], Victor Izquierdo-Roca[1,*]

[1]Catalonia Institute for Energy Research (IREC), Sant Adrià de Besòs-Barcelona 08930, Spain.
[2]Escuela Superior de Física y Matemáticas - Instituto Politécnico Nacional (ESFM - IPN), Ciudad de México 07738, México.
[3]Centres Científics i Tecnològics (CCiTUB) de la Universitat de Barcelona, Barcelona 08028, Spain.
[4]Departament d'Enginyeria Electrònica i Biomèdica, IN2UB, Universitat de Barcelona, Barcelona 08028, Spain.

[*]**Correspondence to:** Dr. Victor Izquierdo-Roca, Catalonia Institute for Energy Research (IREC), Jardins de les Dones de Negre 1, Sant Adrià de Besòs-Barcelona 08930, Spain. E-mail: vizquierdo@irec.cat; Dr. Maxim Guc, Catalonia Institute for Energy Research (IREC), Jardins de les Dones de Negre 1, Sant Adrià de Besòs-Barcelona 08930, Spain. E-mail: mguc@irec.cat

How to cite this article: Fonoll-Rubio, R.; González-Castillo, J. R.; Andrade-Arvizu, J.; Alcobé, X.; Pérez-Rodríguez, A.; Vidal-Fuentes, P.; Guc, M.; Izquierdo-Roca, V. Advancing kesterite absorbers with bronze-based precursors through physical deposition routes: a step toward stable and sustainable industrial photovoltaic technology. *Energy Mater.* **2025**, *5*, 500122. https://dx.doi.org/10.20517/energymater.2024.189

Received: 26 Sep 2024 **First Decision:** 25 Dec 2024 **Revised:** 2 Feb 2025 **Accepted:** 13 Feb 2025 **Published:** 25 Jun 2025

Academic Editor: Chunhui Duan **Copy Editor:** Ping Zhang **Production Editor:** Ping Zhang

Abstract

This work presents, for the first time, a direct comparison of the impact of applying elemental metallic stack precursors and bronze-based precursors to produce $Cu_2ZnSnSe_4$ (CZTSe)-based solar cells by sequential fabrication based on physical deposition methods. Scanning electron microscopy, energy-dispersive X-ray spectroscopy, and X-ray diffraction reveal an improved morphology, a higher compositional homogeneity, and a higher presence of binary alloys in the bronze-based precursor. Scanning electron microscopy observation also shows that bronze-based precursors improve the thickness homogeneity and the rear interface morphology of CZTSe absorbers, while Raman spectroscopy detects an improved crystalline quality and an improved structural micro-homogeneity at the absorber surface. The results of this work also demonstrate that germanium doping, which is required when applying elemental metallic stack precursors, can be avoided in the case of bronze-based precursors without compromising the efficiency of the solar cells. Thus, this work sheds light on the mechanisms induced by bronze-based precursors that contribute to producing high-efficiency CZTSe-based devices, so the

expanded understanding of this precursor can help to further optimize such devices. Additionally, this work demonstrates that the bronze-based precursor reduces material, energy, and time consumption, which favors its possible scaling up to an industrial level.

Keywords: Kesterite, metallic precursor, solar cells, sputtering, technology industrialization

INTRODUCTION

The mass production of large-scale photovoltaic (PV) devices relies on emerging thin-film materials and device architectures built upon stable, environmentally conscious resources. The family of kesterite materials, to which $Cu_2ZnSnSe_4$ (CZTSe) belongs, presents many advantages as absorber layers in thin-film PV devices such as stability, affordability [critical raw materials (CRMs)-free], adaptability to flexible substrates, and tuneable bandgap[1-9]. Its current record energy conversion efficiency [14.9% for $(Ag,Cu)_2ZnSn(S_{1-x}Se_x)_4$] proves its potential for swift industrialization for diverse applications beyond extensive solar farms, including Internet of things, indoor PV, and various emerging paradigms[10-13].

However, the large-scale production of CZTSe-based PV devices presents challenges that must be addressed at early stages of the technology development. It has been reported that the main limitation of kesterite absorbers is the open-circuit voltage (V_{OC}) deficit, which has been attributed to several issues taking place at different parts of the device[14,15]. Among others, the composition and defect properties of the absorber layer have a profound impact on material properties and PV performance, so its precise control is critical[16]. Even subtle compositional deviations can degrade the device efficiency by aggravating defects and grain boundaries, but also special attention has to be given to the inter-grain composition variation, which places a limit in the V_{OC}[15,17,18]. Upscaling magnifies lateral inhomogeneity due to the augmented area-to-thickness ratio, so deposition methods that produce a high uniformity over the device area are required.

The current state of the art of kesterite technologies based on the reactive annealing of a spin-coated Cu_2ZnSnS_4 (CZTS) amorphous precursor has demonstrated the importance of controlling the reaction path from the precursor to the kesterite absorber. It has been reported that reaction paths involving different binary and ternary phases produce a very defective absorber surface and low device efficiencies, while a direct reaction path from the amorphous CZTS precursor to the $Cu_2ZnSn(S_{1-x}Se_x)_4$ (CZTSSe) absorber without intermediate phases produces a high-crystalline-quality absorber with fewer surface defects and higher device efficiencies, including the current record efficiency at the laboratory scale for the kesterite technology[19-21]. However, the chemical-based synthesis technique is limited in its application to an industrial process due to the difficulty in increasing the area and precision of the process. In contrast, precursor deposition via physical routes is more scalable to the industrial level since these routes provide higher control of the process, better reproducibility, and reduced environmental impact since they do not produce chemical residues[22]. In the case of the physical routes, direct deposition of a quaternary phase is not possible, but it has been demonstrated that a reaction path from a precursor to an absorber based on ternary compounds also produces layers with higher crystalline quality and devices with higher efficiencies than reaction paths based on binary compounds[23,24]. Thus, finding homogeneous precursors that can be synthesized through physical routes and promote reaction paths involving as few intermediate phases as possible is critical for scaling up kesterite technology to the industrial level.

Among the different physical routes, deposition by sequential sputtering provides a high control of the precursor structure and composition, and it has produced high-quality kesterite absorbers and high-efficiency devices[22]. Traditionally, an elemental metallic stack precursor is used in the synthesis of

kesterite by sequential physical processes[25]. However, when using such metallic stack precursors, tin and zinc tend to form clusters on the copper layer, leading to an inherently inhomogeneous precursor. Therefore, the search for alternative precursors that eliminate or reduce these inhomogeneities could be a promising path to increase the efficiency and homogeneity of kesterite-based solar cells. Since bronze is an alloy of copper and tin, using it as a precursor material instead of an elemental metallic stack could directly simplify the kesterite synthesis process, thus saving time and energy. Cu-Sn alloy has already been used as a precursor producing CZTSe-based devices in the range of 10% efficiency[26,27]. It has been reported that the alloyed Cu-Sn precursor promotes the beneficial ternary-based reaction pathway to form CZTSe[28,29]. In addition, high efficiencies achieved with the Cu-Sn precursor have been obtained through a single-step annealing process[26,27,29]. Furthermore, synthesizing the CZTSe absorber using a two-step annealing process with the Cu_6Sn_5 alloy as a precursor results in a significant reduction in processing time[30]. In contrast to this, similar efficiencies in the case of elemental metallic stack precursors have been achieved only by applying a relatively long two-step annealing process[15,23,31]. Moreover, the elemental metallic stack precursor requires germanium doping to improve the absorber layer morphology, promote the ternary-based reaction pathway, and achieve high efficiencies[23,31]. Thus, bronze-based precursors provide a high control of the phase formation during the CZTSe synthesis and simplify the annealing process to produce CZTSe-based solar cells while achieving high efficiencies.

In this work, we study the impact of bronze-based precursors on the morphological, structural, and optoelectronic properties of the CZTSe-based solar cells and we compare the obtained results to those achieved in the case of elemental metallic stack precursors to determine which is the optimum precursor when applying physical deposition methods. To the best of our knowledge, this is the first direct comparison of the fundamental differences between elemental and bronze-based precursors reported using the same deposition and annealing equipment. The results show that the bronze-based precursor presents an improved morphology and micro-homogeneity with respect to the elemental Cu/Sn/Cu/Zn metallic stack precursor. In addition, it is also demonstrated that replacing the elemental metallic stack precursor with a bronze-based precursor improves the CZTSe absorber synthesized by physical routes by reducing the structural micro-inhomogeneity present between the grains and by improving the morphology of the absorber layer. This work also examines the effect of germanium doping on the bronze-based precursor, demonstrating that while such doping is necessary for elemental metallic stack precursors to achieve high efficiencies, it can be avoided with bronze-based precursors without any detrimental effects. In consequence, this work demonstrates that bronze-based precursors offer an optimal production process for kesterites through physical routes, marking a significant step toward scaling up CZTSe technology from the laboratory to industrial production scale.

EXPERIMENTAL

CZTSe solar cells analyzed in this work were fabricated through a sequential process. Two types of precursors were produced: an elemental Cu/Sn/Cu/Zn metallic stack precursor and a bronze-based Cu_6Sn_5/Cu/Zn metallic stack one. In both cases, the precursors were deposited by Direct Current (DC) magnetron sputtering (Alliance Concept Ac540) onto a Mo-coated soda lime glass (SLG) substrate. In the case of the metallic stack precursor, and in selected bronze-based precursors for studying the germanium doping impact, a 10 nm Ge nanolayer was evaporated (Oerlikon Univex 250) on top of the precursor. All precursors were reactively annealed under a (Se + Sn) atmosphere in a three-zone tubular furnace to synthetize the CZTSe absorbers. To compare the different precursors, a one-step and a two-step annealing process were applied as detailed in Supplementary Figure 1A. The annealing process was slightly optimized for each precursor, since applying the optimum selenization conditions of the elemental precursor to the bronze-based one results in inefficient devices[30]. To study the impact of the Ge doping on the bronze-based

precursor, a break-off experiment was performed as detailed in Supplementary Figure 1B. After the annealing processes, the obtained absorbers were etched in H_2SO_4 + $KMnO_4$ and $(NH_4)_2S$ solutions to remove the possible presence of secondary phases (mainly ZnSe and SnSe). Next, a CdS buffer layer was deposited via chemical bath deposition (CBD) with a thickness of approximately 50 nm. Then, i-ZnO (50 nm) and In_2O_3:SnO_2 (ITO, 200 nm) layers were deposited by pulsed DC magnetron sputtering (Alliance Concept CT100). The structure of the complete device stack is shown in Figure 1. Finally, 3 × 3 mm^2 cells were mechanically scribed to complete device fabrication and were characterized by measuring both the Current-Voltage (J-V) characteristics under simulated AM1.5 illumination (AAA Abet 3000 Solar Simulator) and the external quantum efficiency (EQE; Bentham Instruments PV300 photovoltaic characterization system).

The samples were characterized by X-ray fluorescence (XRF) for compositional analysis employing a FISCHERSCOPE XVD system calibrated by inductively coupled plasma mass spectrometry. Scanning electron microscopy (SEM; ZEISS Series Auriga microscope) was used for the morphological analysis by applying a 5 kV accelerating voltage and a working distance of 4-7 mm. The same system was employed to measure SEM energy-dispersive X-ray spectroscopy (EDX), but applying a 20 kV accelerating voltage. X-ray diffraction (XRD) measurements were performed using a PANalytical X'Pert PRO MPD alpha1 diffractometer in a Bragg-Brentano θ/2θ configuration with Cu K_{α_1} radiation (λ = 1.5406 Å), selected by means of a Johanson type Ge (111) focusing primary monochromator. For the comparative study of the elemental and bronze precursors, macro-Raman spectroscopy was measured under 325 nm and 532 nm excitations on a 4 × 4 mm^2 area of the CZTSe absorbers with laser spot diameters around 70 μm, which ensures that the obtained data is representative of the sample. Then, micro-Raman spectroscopy was measured under 325 nm and 532 nm excitations on a 50 × 50 μm^2 area with a laser spot size of around 1 μm^2 and with a step size of 10 μm, conditions that ensured that each individual measured point corresponded to a different CZTSe grain. For the study of the impact of Ge doping, multiwavelength macro-Raman characterization was performed using lasers with excitation wavelengths of 442 nm, 532 nm, and 785 nm. In all cases, Raman spectroscopy measurements were carried out in backscattering configuration using a Horiba Jobin Yvon fHR-640 spectrometer for 325 nm, 442 nm and 532 nm wavelengths, and an iHR-320 spectrometer for the 785 nm wavelength. In order to avoid thermal effects in the spectra, the power density on the surface of samples was kept below 150 W/cm^2. The position of all spectra was corrected by measuring the first order Raman spectrum of monocrystalline silicon and imposing its position to 520 cm^{-1}. To analyze the rear interface by SEM and Raman spectroscopy, a mechanical lift-off procedure was performed as shown in Supplementary Figure 1C. Finally, photoluminescence (PL) spectroscopy was measured under 633 nm excitation in a backscattering configuration using a Sol 1.7 spectrometer from B&WTek with an InGaAs detector.

RESULTS AND DISCUSSION

Comparative study of elemental metallic stack and bronze-based precursors

In this section, a bronze-based precursor will be compared to an elemental metallic stack to uncover the fundamental differences between them and the precursor characteristics that influence the CZTSe growth. Then, the same deposition and annealing equipment is employed to produce CZTSe absorbers and devices from both bronze-based and elemental metallic stack precursors, which will allow a direct comparison between them to shed light on the impact of the bronze-based precursors on the morphological, structural, and optoelectronic properties of the CZTSe-based solar cells.

Precursor analysis

Here, the differences in the morphology, composition, and phase formation between an elemental metallic

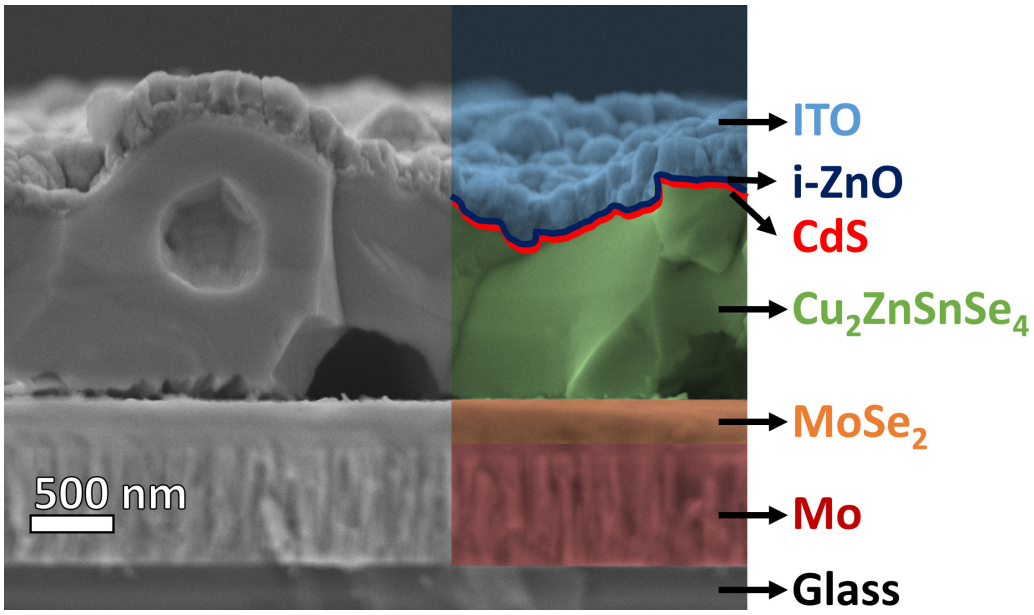

Figure 1. Cross-sectional SEM image of the representative stack structure of CZTSe-based devices studied in this work. Each layer of the stack is identified. SEM: Scanning electron microscopy; CZTSe: $Cu_2ZnSnSe_4$.

stack precursor and a bronze-based precursor will be elucidated. Table 1 shows that the global composition measured by XRF of both precursors is almost equal (considering the experimental error of the equipment), which eliminates any possible difference between precursors due to compositional variations and ensures that the extracted conclusions of the comparison are due to the intrinsic differences between both processes.

Figure 2A and B show a comparison between the elemental metallic stack precursor and the bronze-based precursor by cross-sectional SEM images and their corresponding EDX elemental maps are shown in Figure 2C and D. In the case of the elemental metallic stack precursor, shown in Figure 2A, SEM and EDX observation of the cross-section reveals an irregular morphology due to the formation of Sn islands that affect the distribution of the Cu and Zn upper layers. Line profiles obtained from the EDX maps for this precursor, which are shown in Figure 2C, reveal a formation of a bilayer structure consisting of a Zn-rich layer at the top and a Sn-rich layer at the bottom. It is fair to assume that this inhomogeneity that can be found already in the precursor will generate further micro-homogeneity problems in the annealed absorbers. Here, it is worth noting that alternative orders of the elemental metallic stack, such as Zn/Sn/Cu and Zn/Cu/Sn, were reported to produce poor absorber morphologies, so this is a common limitation of the elemental precursor[32]. In the case of the bronze-based precursor, shown in Figure 2B, SEM and EDX reveal a regular, flat surface with each elemental layer very well defined. This indicates that Cu_6Sn_5 has a higher wettability than Sn on the Mo-coated substrate, so replacing the Cu/Sn/Cu/Zn precursor with a Cu_6Sn_5/Cu/Zn precursor changes the nucleation from an island growth to a layer-by-layer one, which results in an improved precursor morphology and lateral homogeneity. Nevertheless, the bilayer structure with a Zn-rich top and a Sn-rich bottom that was detected in the elemental metallic stack precursor is also observed in the bronze-based precursor, as shown in the line profile from the EDX maps in Figure 2D. This bilayer structure is determined by the sputtering order of the targets, suggesting that some inhomogeneities along the depth of the absorber layer may still occur when using a bronze-based precursor. Co-sputtering deposition of the kesterite precursor could improve the in-depth homogeneity, but this technique can produce cross-contamination of the targets that hinders the synthesis process, and the amount of studies published in the literature reporting high-efficiency devices is limited compared to the sequential sputtering

Table 1. Elemental atomic ratios obtained by XRF of an elemental metallic stack precursor and a bronze-based precursor

Precursor	[Cu]/([Zn]+[Sn])	[Zn]/[Sn]
Elemental	0.73 ± 0.02	1.11 ± 0.02
Bronze	0.71 ± 0.02	1.14 ± 0.02

XRF: X-ray fluorescence.

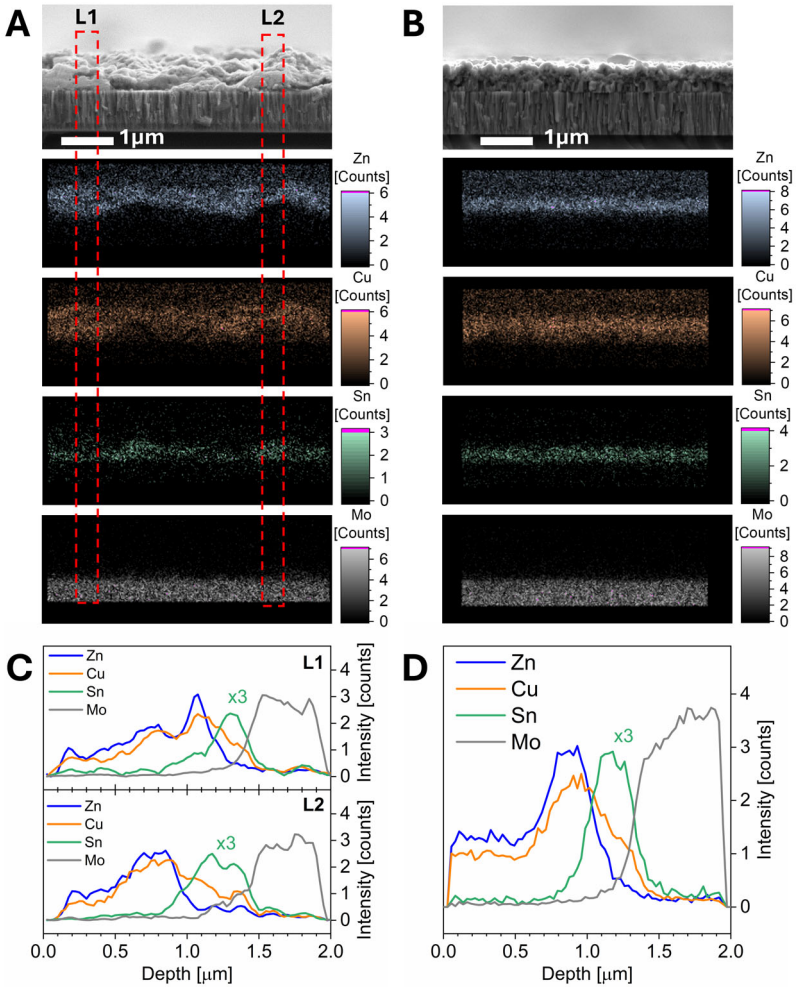

Figure 2. Cross-sectional SEM images and their corresponding Zn, Cu, Sn, and Mo EDX elemental maps of (A) an elemental metallic stack precursor and (B) a bronze-based precursor. From the EDX maps, line profiles of the intensity of each element along the depth of the precursor are obtained; For the elemental metallic stack precursor (C), two profiles are obtained: one from a region where the Sn layer is thinner (L1) and one from a region where this layer is thicker (L2); For the bronze-based precursor (D), only one profile is obtained due to the high lateral homogeneity, which is the average along all the width of the sample. SEM: Scanning electron microscopy; EDX: energy-dispersive X-ray spectroscopy.

deposition, especially for the pure selenide kesterite compounds[22].

Figure 3 shows the XRD patterns of the elemental metallic stack precursor and the bronze-based precursor in a selected range where relevant peaks were detected (full range can be observed in Supplementary Figure 2). The presence of metallic Sn, Cu-Sn phase (e.g., Cu_6Sn_5), and Cu-Zn phase (e.g., Cu_5Zn_8) is detected by XRD in the elemental metallic stack precursor, indicating that Cu reacts with both Sn and Zn during the

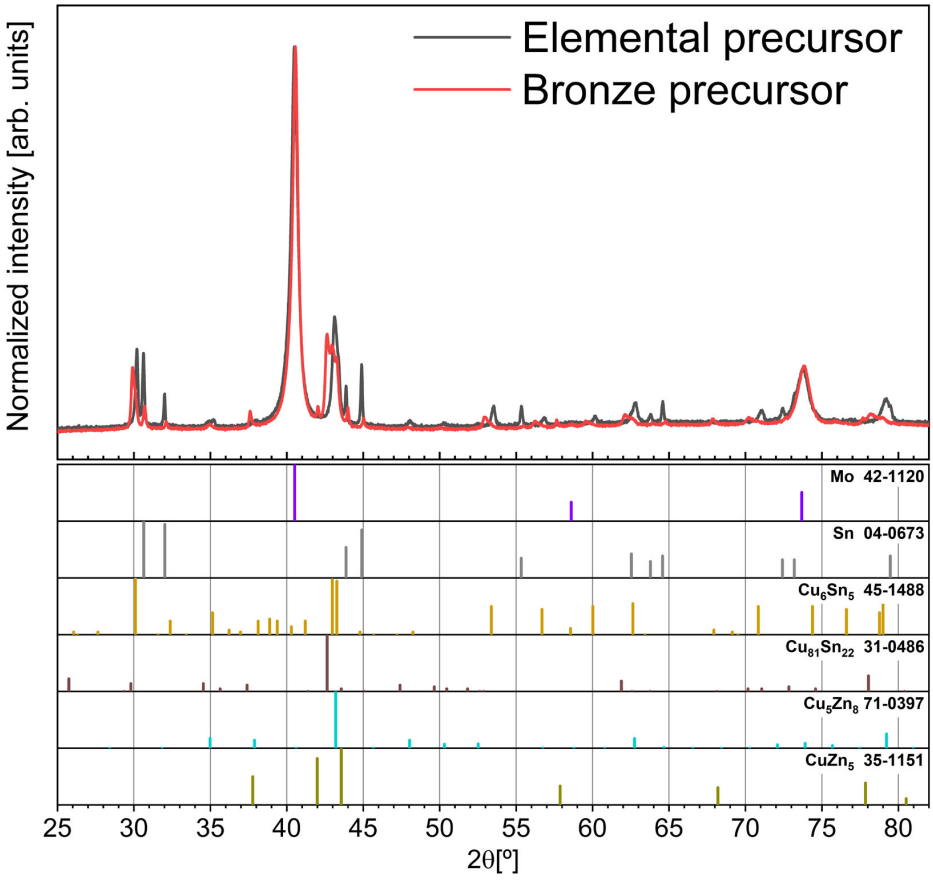

Figure 3. X-ray diffractograms of the elemental metallic stack precursor and the bronze-based precursor. Diffractograms are normalized to Mo reflection peak at 40.5°. Under the measured diffractograms, the patterns of different phases detected in the precursors are listed and the numbers behind each phase correspond to reference patterns in ICDD database. ICDD: International centre for diffraction data.

sputtering deposition of the elemental metallic stack. The detection of a Cu-Sn binary phase indicates that this phase plays a role in the formation of CZTSe even when an elemental metallic stack precursor is applied, so this justifies the replacement of such a precursor by a bronze-based one, since having the Cu_6Sn_5 phase already present in the sputtering target would provide a higher control over this phase. In the bronze-based precursor, Cu-Sn (e.g., Cu_6Sn_5 and $Cu_{81}Sn_{22}$,) and Cu-Zn (e.g., $CuZn_5$) binary phases are detected by XRD; there is also presence of metallic Sn, but its signal is considerably lower than in the case of the elemental metallic stack precursor. In consequence, applying a bronze-based precursor promotes a precursor with a higher presence of binary phases and a lower presence of single elements, which, according to previous studies, plays a critical role in controlling the formation pathway of CTZSe[23,24,33,34]. Finally, considering the bilayer structure consisting of a Zn-rich top and Sn-rich bottom observed in both precursors in Figure 2C and D, it is expected that Cu-Zn binary phases detected by XRD are located at the surface of the precursors, while the Cu-Sn binary phases are located at the bottom side.

The comparison between an elemental metallic stack precursor and a bronze-based precursor by SEM, EDX, and XRD reveals that applying a bronze-based precursor improves the morphology and the lateral compositional micro-homogeneity of the precursor, and it also promotes a higher presence of binary compounds in the precursor. The impact of these improvements on the compositional, morphological, and structural properties of the CZTSe absorber after the selenization of the precursor and their impact on the

optoelectronic parameters of the final device is analyzed in the next sections.

Impact on the CZTSe absorber properties

This section studies the impact of the bronze-based precursor on the compositional, morphological, and structural properties of CZTSe absorbers as compared to the impact of the elemental metallic stack precursor. To perform this analysis, the elemental metallic stack precursor was selenized by applying the two-step annealing process that was employed in high-efficiency CZTSe-based devices produced from this type of precursor[15,23,31]. Regarding the bronze-based precursor, two different annealing processes were applied (see Supplementary Figure 1A). On one side, it was applied a one-step annealing process, which is the strategy that produced the reported high-efficiency CZTSe-based devices fabricated from alloyed Cu-Sn precursors[26,27,29,33]. On the other hand, to ensure that the obtained results are due to the different precursors instead of the different annealing processes, it was also applied a two-step annealing process.

Table 2 shows the elemental atomic ratios obtained by XRF for CZTSe absorbers synthesized from an elemental metallic stack precursor and from bronze-based precursors employing the same deposition and annealing systems. It can be observed that, regardless of the type of precursor and the number of steps of the annealing process, the produced CZTSe absorbers show Cu-poor and Zn-rich compositions, which are required to obtain high-efficiency CZTSe-based solar cells[15,18,23,27,35,36]. However, applying a two-step annealing process produces practically the same compositions for both elemental and bronze-based precursors, while applying a one-step process to the bronze-based precursor produces an absorber with a slightly more Cu-poor and a more Zn-rich composition. This indicates that, having similar precursor compositions, the final composition of the CZTSe absorber depends on the annealing process rather than on the type of the precursor. A possible explanation for the higher [Zn]/[Sn] ratio when applying the one-step process can be associated with the elemental Sn added in the graphite box to compensate for its loss during the annealing process. This approach works similarly for the two-step process independently on the precursor type, but for the one-step process, Sn loss may prevail over the compensation rate of the added elemental Sn. Thus, either a higher amount of Sn should be added in the graphite box or the composition of the bronze-based precursor should be changed towards the less Zn-rich side to achieve a [Zn]/[Sn] ratio similar to the one obtained by the two-step annealing process.

SEM micrographs of various regions of CZTSe absorbers synthesized from an elemental metallic stack precursor and from bronze-based precursors are shown in Figure 4. Focusing first on the case of the elemental metallic stack precursor, it can be observed that large CZTSe grains (covered by the nanometric buffer and window layers) are formed producing a high surface roughness, so the points with reduced thickness (< 1.5 μm) will not collect the long wavelength photons and thus will reduce the short-circuit current density (J_{SC})[15,37-40]. Additionally, a significant number of voids are observed at the rear interface of the absorber, with the contact area between CZTSe and $MoSe_2$ being approximately 40%. The presence of such voids at the back interface of CZTSe absorbers has been extensively reported in the literature, and it is associated with a reduction of the fill factor (FF) and J_{SC} of the final devices[14,15,23,41,42]. Considering the morphology and compositional micro-inhomogeneity of the elemental metallic stack precursor observed in Figure 2A-D, the high surface roughness of the absorber and the significant presence of voids at the back interface can be attributed to the irregular distribution of the metallic Sn layer in the precursor. This irregularity may lead to a bilayer structure during the annealing process, increasing thickness inhomogeneity and promoting the formation of volatile Sn-Se secondary phases at the back interface. When a bronze-based precursor is used, large CZTSe grains are also formed, with some exceeding 5 μm^2 in size. However, in this case, the absorber surface is smoother compared to when an elemental metallic stack precursor is applied. This reduction of the surface roughness is achieved by both one-step and two-step

Table 2. Elemental atomic ratios obtained by XRF for CZTSe absorbers synthesized from an elemental metallic stack precursor and from bronze-based precursors. In the second case, different absorbers were synthesized by applying a one-step and a two-step annealing process

Precursor	Annealing process steps	[Cu]/{[Zn]+[Sn]}	[Zn]/[Sn]
Elemental	Two	0.76 ± 0.02	1.07 ± 0.02
Bronze	One	0.72 ± 0.02	1.18 ± 0.02
Bronze	Two	0.75 ± 0.02	1.09 ± 0.02

XRF: X-ray fluorescence; CZTSe: $Cu_2ZnSnSe_4$.

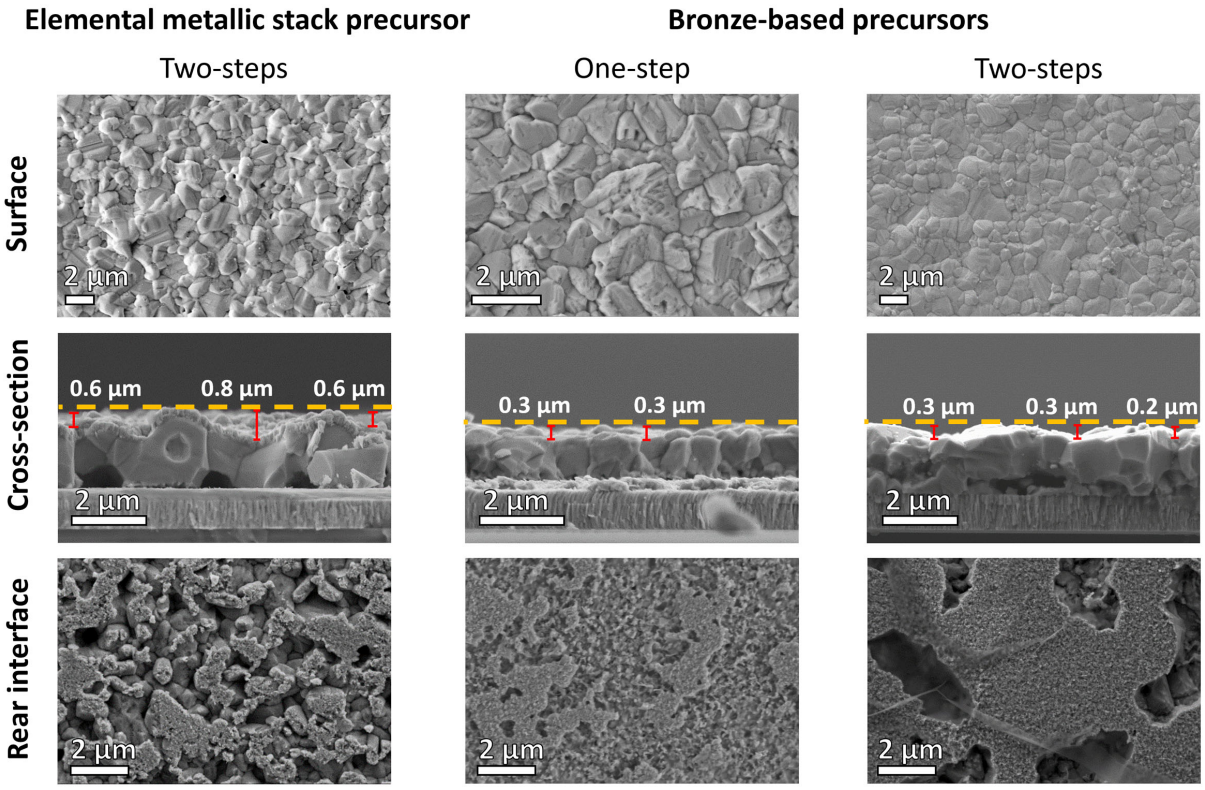

Figure 4. SEM images obtained at the surface, cross-section, and rear interface of CZTSe absorbers synthesized from an elemental metallic stack precursor and from a bronze-based precursor. SEM: Scanning electron microscopy; CZTSe: $Cu_2ZnSnSe_4$.

annealing processes, so this improvement can be assigned to the precursor configuration, and it can be explained by the smoother surface of the bronze-based precursor and its high lateral micro-homogeneity observed in Figure 2C and D. The improved homogeneity of the absorber layer thickness when applying bronze-based precursors can improve the quality of the CdS layer deposited on top and therefore reduce space charge region fluctuations and shunting, thus improving V_{OC} and FF, and it can improve the absorption of the near-infrared photons, which would increase the J_{SC}[15,37-40]. Focusing on the cross-sectional observation of the rear interface, the large voids are not observed when applying a one-step annealing process to the bronze-based precursor and, in their place, a bilayer structure is formed with small CZTSe grains below the large CZTSe grains (see Supplementary Figure 3). The presence of the small CZTSe grains increases the number of grain boundaries at the CZTSe/$MoSe_2$ interface, which can increase the recombination losses, reduce the FF and J_{SC} of the device due to increased series resistance, and reduce its stability due to a weaker attachment of the absorber layer to the back contact[15]; however, this effect will be

enhanced by the formation of voids. The bilayer structure of the rear interface in the case of the one-step process contrasts with the structure observed when applying the two-step annealing process to the bronze-based precursor. In this case, despite some small grains being observed, the bilayer structure is not so well defined, and, in addition, big voids are observed as in the case of the elemental metallic stack precursor. The one-step annealing process produces a full contact area, although it has to be taken into account that this contact with the $MoSe_2$ layer is mostly produced by the small grains [Figure 4]. When the two-step annealing process is applied to the bronze-based precursor, the voids observed at the rear interface are larger than in the case of the elemental metallic stack precursor, but their number is lower, which results in an increased contact area between CZTSe and $MoSe_2$ around 75%, and this reduces the Schottky barriers at the back interface[15,43]. Thus, SEM observation shows that the structure of the rear interface when applying a bronze-based precursor depends on the annealing process; however, there are characteristics that can be observed for both applied annealing processes, so their origin can be assigned to the bronze-based precursor. Specifically, the bronze-based precursor produces a more homogeneous morphology of the rear interface than the elemental metallic stack precursor, with a lower presence of voids and an increased contact area between the absorber and the $MoSe_2$ layer. The absence or reduction of voids at the rear interface when applying a bronze-based precursor, along with the more homogeneous morphology of such interface, can be explained by the homogeneous lateral distribution of Sn in the precursor [Figure 2A and B] and by the fact that this Sn is mainly alloyed with Cu [Figure 3], so the lower presence of elemental Sn in the precursor avoids the formation of volatile Sn-Se secondary phases during the annealing process that reduces the formation of voids at the rear interface of the CZTSe absorber.

The structural quality of the CZTSe absorbers was studied by means of macro-Raman spectroscopy. Figure 5 shows different parameters obtained from the Raman spectra measured under 325 nm and 532 nm excitation wavelengths in CZTSe absorbers synthesized from an elemental metallic stack precursor and from bronze-based precursors (the corresponding spectra are shown in Supplementary Figures 4 and 5). Following the previous studies, the spectra measured under 325 nm excitation were used to estimate the concentration of copper vacancies (V_{Cu}) and zinc-on-tin antisites (Zn_{Sn}) point defects inside the CZTSe by calculating the relative integrated intensity of the peaks at 175 cm^{-1} and 250 cm^{-1}, respectively[44]. The spectra measured under 532 nm excitation were used to evaluate the crystalline quality of the CZTSe by calculating the full width at half-maximum (FWHM) of the Raman peak at 196 cm^{-1}[16]. Figure 5A shows that the relative integrated intensity of the 175 cm^{-1} Raman peak of the CZTSe phase increases when applying a bronze-based precursor and a one-step annealing process, which corresponds to a lower density of V_{Cu} inside the CZTSe structure compared to the elemental metallic stack precursor case[44]. When applying a two-step process to the bronze-based precursor, the difference with respect to the elemental metallic stack precursor is strongly reduced, with only a slightly decreased density of V_{Cu}; however, this small difference can produce notable variations in the optoelectronic properties of the devices[44]. Figure 5B shows the relative integrated intensity of the 250 cm^{-1} peak, which also increases when applying a bronze-based precursor and a one-step annealing process, indicating an increase of the Zn_{Sn} density in the CZTSe absorber[44]. Applying a two-step annealing process to the bronze-based precursor reduces the difference with the elemental metallic stack precursor, but the Zn_{Sn} density is still slightly higher, and this can produce a noticeable negative impact on the optoelectronic parameters[44]. In order to compare the results of defect density variation in different absorbers with their chemical composition [Table 2], it is important to notice that the applied excitation wavelength (325 nm) results in a strong sensitivity of Raman spectroscopy to the surface of the absorbers due to its low penetration depth (tens of nm), while the XRF technique, used for the chemical composition estimation, provides average information from the whole bulk of the absorber. Bearing this in mind, the increased amount of Zn_{Sn} density in the absorber made by applying bronze-based precursor and one-step annealing agrees with the increased [Zn]/[Sn] ratio, which indicates a similar depth distribution of this defect for all absorbers. On the contrary, the slightly decreased value of [Cu]/{[Zn]+[Sn]}

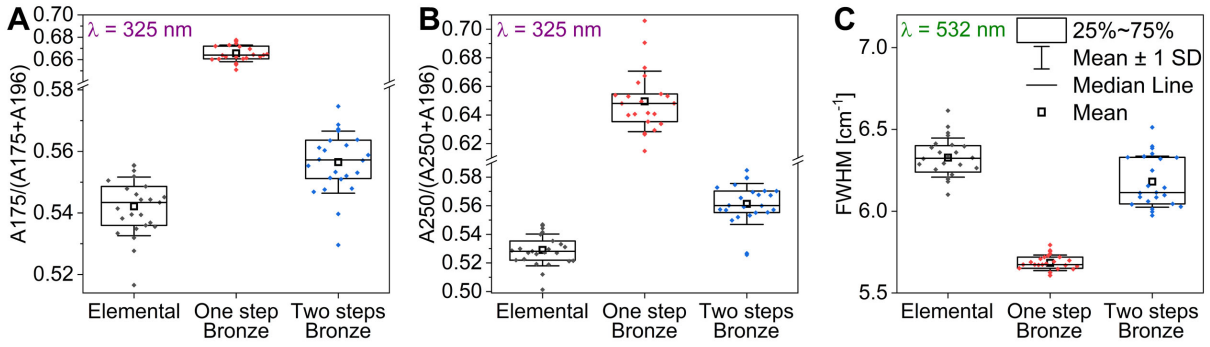

Figure 5. (A) Relative area of the 175 cm^{-1} peak; (B) relative area of the 250 cm^{-1} peak, and (C) full width at half-maximum of the 196 cm^{-1} peak obtained by macro-Raman spectroscopy under 325 nm and 532 nm excitations on CZTSe absorbers synthesized from an elemental metallic stack precursor and from bronze-based precursors. In the second case, different absorbers were synthesized by applying a one-step and a two-step annealing process. CZTSe: $Cu_2ZnSnSe_4$.

in the absorber made by applying bronze-based precursor and one-step annealing looks controversial to the observed decreased density of V_{Cu} at the absorber surface. This can be explained only by the increased inhomogeneity in the distribution of this defect in the bulk of this absorber compared to others, i.e., lower concentration in the surface and higher in the bulk, and can be associated with the double layer structure of this absorber observed in the SEM cross-section image [Figure 4]. Finally, Figure 5C shows that the FWHM of the 196 cm^{-1} peak changes insignificantly in the analyzed absorbers, being already small for the absorber made from the elemental precursor, and it is only slightly improved in absorbers made from bronze-based precursors[16]. Additionally, to other techniques, PL spectroscopy was performed on the CZTSe absorbers [Supplementary Figure 6] and it revealed slightly different energy positions of the PL emission for each sample, being higher for the elemental case. Similar variations in the PL emission energy have been previously detected by different researchers, and were associated with the variation in the Cu/Zn disorder and/or in the structural defects concentration[16,34], which agrees with the above Raman spectroscopy analysis. Taking into account these results, it can be concluded that variations of the chemical composition and the annealing process play a crucial role for both elemental and bronze-based precursors, and, even if the Cu-Sn alloy implies a restriction on the chemical composition with respect to depositing elemental layers, these parameters can be controlled in the bronze-based precursor to obtain an optimal amount of absorber defects and/or their distribution in the same way as in the elemental precursor.

Additionally, the structural micro-homogeneity of the CZTSe absorbers was analyzed by micro-Raman spectroscopy under the same 325 nm and 532 nm excitation wavelengths [Supplementary Figures 7 and 8] measuring in conditions that guaranteed that each measured point corresponded to practically an individual absorber grain (see Experimental section for details). In this case, the same three parameters as discussed above have been evaluated; however, the focus was not on the variation of average values between samples (which were similar to the results of macro-Raman, compare Figure 5 and Supplementary Figure 9), but on the variation of these parameters inside each sample. This was expressed by the coefficient of variation (CV) value, a standardized measurement of the dispersion of a value. Table 3 shows the CV of three different parameters obtained from the micro-Raman spectra. It can be observed that, when applying a one-step annealing process to the bronze-based precursor, the three analyzed parameters present the lowest CV values. Since the CV quantifies the data dispersion, this indicates improved inter-grain homogeneity of the CZTSe absorber, which should be beneficial for the V_{OC} of the devices[15], and this improvement is a consequence of the higher lateral compositional micro-homogeneity of the bronze-based precursor that was observed by SEM-EDX in Figure 2A and B. However, the improvement of the structural micro-homogeneity is not observed when applying the two-step annealing process, so it cannot be

Table 3. Coefficient of variation of the relative area of the 175 cm^{-1} and 250 cm^{-1} peaks, and of FWHM of 196 cm^{-1} peak calculated from the spectra of micro-Raman measured under 325 nm and 532 nm excitations in different CZTSe absorbers

Precursor	Annealing process steps	CV of $A_{175}/(A_{175}+A_{196})$ [%]	CV of $A_{250}/(A_{250}+A_{196})$ [%]	CV of $FWHM_{196}$ [%]
Elemental	Two	2.2	8.1	0.7
Bronze	One	1.9	2.4	0.5
Bronze	Two	2.6	7.6	1.4

CZTSe: $Cu_2ZnSnSe_4$; CV: coefficient of variation; FWHM: full width at half-maximum.

discarded that the impact of the annealing process on the inter-grain homogeneity is comparable to the effect of the precursor. In any case, since the reported high-efficiency CZTSe-based solar cells produced from bronze-based precursors were fabricated by applying a one-step annealing process[26,27], it is plausible that such devices benefited from the improved structural micro-homogeneity detected in this work. Moreover, the improved structural micro-homogeneity could explain the enhanced reproducibility in the fabrication of high-efficiency CZTSe-based devices, as well as the promising efficiencies in large area devices, which are reported in the literature when applying bronze-based precursors[26].

The comparison of CZTSe absorbers synthesized from different precursors shows that, regardless of the annealing process, the bronze-based precursor improves the absorber morphology with respect to the elemental metallic stack precursor. Specifically, it reduces the surface roughness and, additionally, reduces the number of voids at the back interface of the absorber, thus increasing the contact area between CZTSe and $MoSe_2$. Moreover, the bronze-based precursor produces CZTSe absorbers with slightly better crystalline quality at the surface, and the amount and distribution of the point defects can be controlled as well as in absorbers made from elemental precursors. Finally, the lateral micro-homogeneity of the CZTSe structure quality could be improved by applying the optimal annealing conditions. In the next section, it will be analyzed whether the improved morphology and micro-homogeneity obtained when applying a bronze-based precursor translate to an improvement of the optoelectronic properties of the solar cells.

Effect on optoelectronic parameters

The CZTSe absorbers synthesized from elemental metallic stack and bronze-based precursors were used to produce solar cell devices. Figure 6 shows the comparison between the different optoelectronic parameters of the produced solar cells. The current density-voltage of the cells that achieved the highest efficiencies and the EQE curves of the cells that presented the highest integrated EQE are shown in Supplementary Figure 10. In Figure 6A, it can be observed that, although the elemental metallic stack precursors produce a few cells with a higher J_{SC}, the robust statistics such as the median value and the interquartile range show an improvement of the J_{SC} when applying the bronze-based precursor regardless of the utilized annealing process. The improvement of the J_{SC} when applying a bronze-based precursor can be explained by the improved homogeneity of the absorber layer thickness and the reduction of voids at the rear interface observed in Figure 4, which increase the absorption of the near-infrared photons, as also detected by EQE measurements shown in Supplementary Figure 10B[14,15,23,37-42]. However, in this study, the elemental metallic stack precursor produced devices with a considerably higher V_{OC} and a higher FF, as shown in Figure 6B and C, respectively, which resulted in higher energy conversion efficiencies for such elemental precursors, as shown in Figure 6D.

The lower efficiencies achieved by bronze-based precursors in this work are contradictory with the observed improvements in the morphology, structure, and homogeneity of the absorber, but this can be explained by

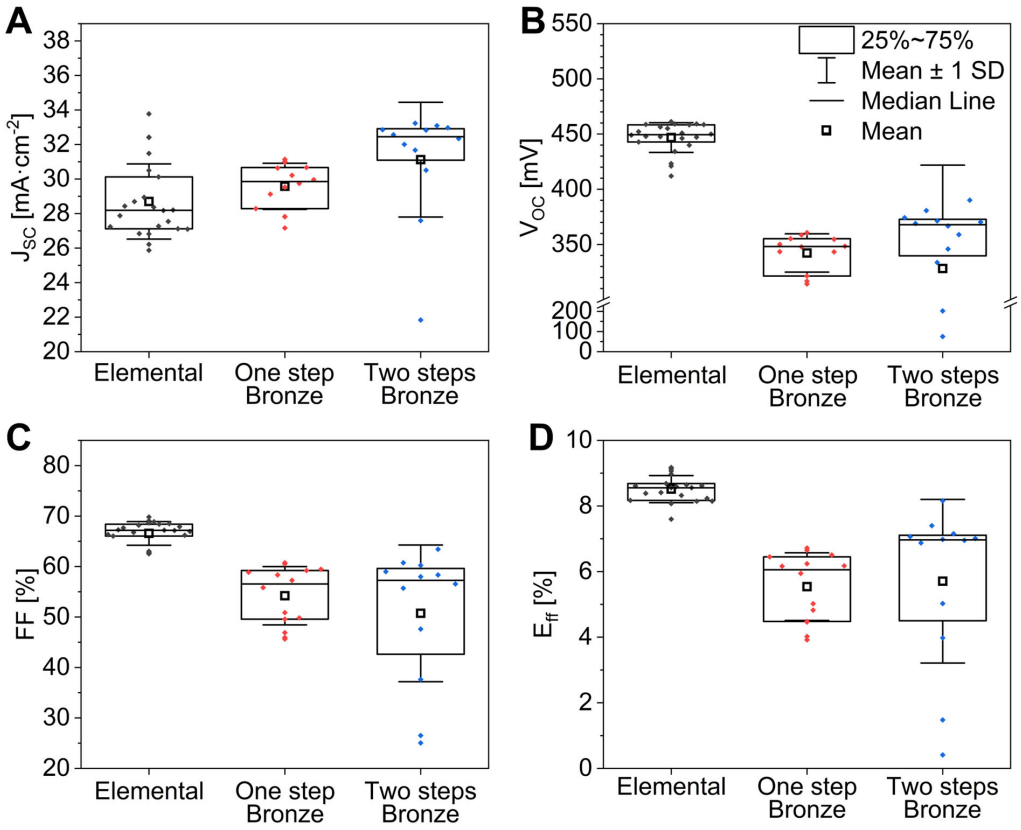

Figure 6. (A) Short-circuit current density; (B) open-circuit voltage; (C) fill factor, and (D) energy conversion efficiency of CZTSe-based solar cells synthesized from an elemental metallic stack precursor and from bronze-based precursors. In the second case, different absorbers were synthesized by applying a one-step and a two-step annealing process. CZTSe: $Cu_2ZnSnSe_4$.

the state of optimization of the fabrication process for each precursor using the deposition and annealing equipment employed in this work. First, the low V_{OC} and FF values obtained in this study when applying bronze-based precursors could be partially explained by the lower V_{Cu} point defect density and the higher Zn_{Sn} point defect density detected by Raman spectroscopy in Figure 5[44]. Here, it is important to note that, to discard the influence of compositional variations, both elemental metallic stack and bronze-based precursors were synthesized with the same composition, as shown in Table 1. While this precursor composition produced high-efficiency CZTSe-based solar cells when applying an elemental metallic stack precursor and a two-step annealing process[15,23,31], it is fair to assume that the precursor composition has to be optimized when varying the precursor to a bronze-based one, and a further optimization should be performed when varying the annealing process to a one-step process. In addition, the CdS, the i-ZnO, and the ITO layers, whose deposition was optimized for the elemental precursor, might be far from optimal for the bronze-based precursor, resulting in detrimental buffer and window layers that contribute to the V_{OC} and FF decrease. Thus, an optimization of the precursor composition, the annealing process, and the buffer and window layers can lead to higher device performances when applying the bronze-based precursor, as demonstrated by the efficiencies higher than 11% achieved in the literature when applying this precursor[26,27]. Additionally, the literature also reports that applying bronze-based precursors has produced some of the lowest V_{OC} deficits achieved in the CZTSe technology[27,33], and this reduction of the V_{OC} deficit could be explained by the improved structural micro-homogeneity of the CZTSe absorber and by the improved thickness homogeneity of the absorber layer presented in this work[15,37-40]. While the efficiencies achieved by the bronze-based precursor in this work are not higher than the ones achieved by the elemental

metallic stack precursor, the direct comparison of both precursors studied here allowed the identification of positive modifications induced by the bronze-based precursor that can contribute to the high efficiencies reported in the literature[26,27], helping to better understand this precursor and opening the way for the further optimization of the CZTSe-based devices produced from it.

Ge-doping impact on bronze-based precursors

In the case of the elemental metallic stack precursor synthesized by physical routes, doping the precursor with a germanium nanolayer produced an improvement of the efficiency of CZTSe-based solar cells due to a modification of the absorber formation pathway and its crystallization[23,31]. In the case of the alloyed Cu-Sn precursor, the highest efficiencies have been achieved from Ge-free precursors[26,27,29], but, up to our knowledge, there are no reported studies on the impact of Ge-doping on bronze-based precursors. In consequence, this section analyzes if Ge doping has the same positive impact on bronze-based precursors as it has on elemental metallic stack precursors or, contrastingly, if this doping can be avoided when applying bronze-based precursors.

Influence on the reaction pathways to form CZTSe

To study the impact of Ge doping on the CZTSe formation pathways when alloyed Cu-Sn precursors are applied, bronze-based precursors with no germanium (Ge-free precursor) and with a 10 nm germanium layer deposited on its top (Ge-doped precursor) were annealed in a selenium atmosphere by performing a break-off experiment as detailed in Supplementary Figure 1B.

Figure 7 shows the evolution with the annealing process of the [Zn]/[Sn] and [Cu]/{[Zn]+[Sn]} elemental atomic ratios obtained by XRF measured on samples obtained from Ge-free and from Ge-doped bronze-based precursors. When annealing the Ge-free precursor, it can be observed that the value of both elemental atomic ratios increases until the annealing temperature reaches 400 °C, indicating a loss of Sn in the absorbers during this stage of the annealing process. This Sn-loss during the CZTSe synthesis has been widely reported and is associated with the volatility of Sn-Se phases[23,45-48]. For the Ge-doped precursor, the ratios also increase at the earliest stage of the annealing process, so a Sn loss also occurs in this case. However, at 400 °C and 450 °C, the elemental atomic ratios are considerably lower when applying a Ge-doped precursor than applying a Ge-free one, which indicates that doping the bronze-based precursor with germanium reduces the loss of Sn at the earlier stages of the annealing process. For annealing temperatures higher than 450 °C, the value of both elemental atomic ratios decreases in the case of the Ge-free precursor, indicating that the Sn loss is compensated at these process stages by the evaporation of the melted elemental Sn added in the graphite box. For the Ge-doped precursor, the evolution of these ratios becomes more irregular at temperatures above 450 °C, generally showing a decreasing trend, which indicates that Sn loss is also compensated in this case. However, an increase in the ratios is observed during the final stage of the process. Thus, at the end of the annealing process, the absorber annealed from a Ge-free precursor presents [Zn]/[Sn] = 1.18 and [Cu]/{[Zn]+[Sn]} = 0.72, while the absorber annealed from the Ge-doped precursor presents [Zn]/[Sn] = 1.21 and [Cu]/{[Zn]+[Sn]} = 0.72. This indicates that, although the Ge-free precursor produces a higher Sn loss at the earlier stages of the annealing process, the composition of the final absorber is similar for both types of bronze-based precursors. In fact, the Ge-doped precursor produces a slightly higher [Zn]/[Sn] ratio for the final absorber, so the loss of Sn at the end of the annealing process is slightly higher when doping the precursor with germanium.

Analysis of the phase formation at different synthesis temperatures was performed by means of Raman spectroscopy measured under different excitation wavelengths (442 nm, 532 nm and 785 nm), which enhances the signal of different phases. Figure 8 shows the obtained Raman spectra of the absorbers

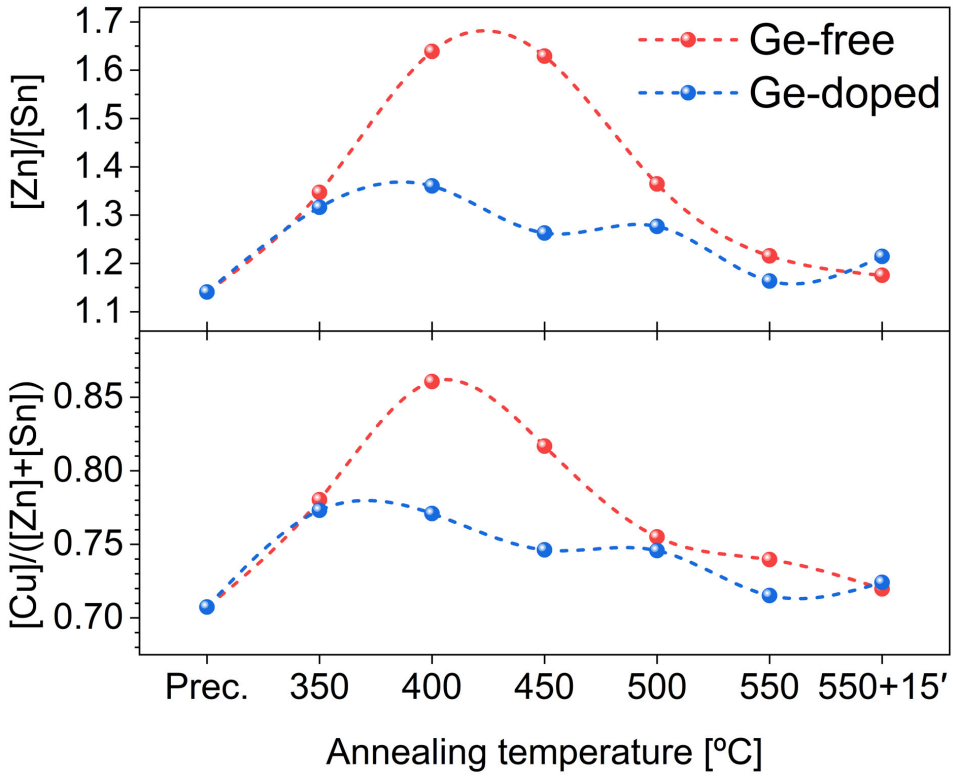

Figure 7. Evolution of the [Zn]/[Sn] and [Cu]/{[Zn]+[Sn]} elemental atomic ratios obtained by XRF measured on samples synthesized from Ge-free and Ge-doped bronze-based precursors at different stages of a one-step annealing process. XRF: X-ray fluorescence.

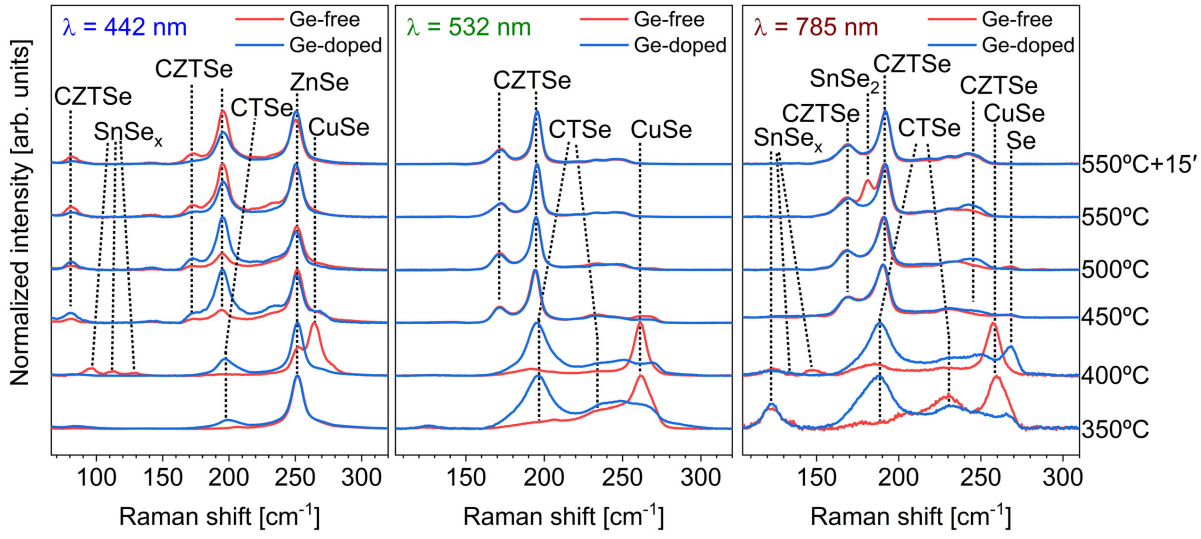

Figure 8. Raman spectra measured under 442 nm, 532 nm, and 785 nm excitation wavelengths of absorbers produced at different stages of a one-step annealing process from Ge-free and Ge-doped bronze-based precursors. Each spectrum is normalized to the maximum peak of the corresponding spectrum.

produced from Ge-free and Ge-doped bronze-based precursors at the different stages of the annealing process. Focusing on the Ge-free precursor, binary (ZnSe, CuSe, $SnSe_x$) and ternary (Cu_2SnSe_3) compounds

are detected at the first stages (350 °C and 400 °C). The detection of $SnSe_x$ Raman peaks at the absorber surface at lower annealing temperatures, along with their absence at higher temperatures, agrees with the evaporation of this phase and with the Sn-loss during the initial stages, as corroborated by XRF results in Figure 7. The formation of the Cu_2SnSe_3 ternary phase at these early stages of the annealing process when applying Ge-free bronze-based precursors is in agreement with the literature[28,29], indicating that the bronze-based precursor promotes a reaction pathway to form CZTSe through the ternary compound, something that has been reported to be beneficial for the production of high-efficiency CZTSe-based devices[19,20,23]. The formation of the CZTSe phase is first detected for an annealing process temperature of 450 °C. For higher annealing temperatures, the crystalline quality of the CZTSe phase improves, as indicated by the reduction of the width of the corresponding Raman peaks, and the intensity of peaks of the secondary phases detected at earlier stages is reduced or the peaks disappear. At the end of the annealing process, the only secondary phase that is detected at the surface of the absorber is ZnSe, which is coherent with the Zn-rich composition measured by XRF. When applying a Ge-doped precursor, ZnSe, CuSe and Cu_2SnSe_3 are also detected at the first process stages. In this case, however, the relative intensity of the peaks of the ternary compound compared to the binary compounds is significantly higher than in the case of the Ge-free precursor, suggesting that Ge doping in the bronze-based precursor accelerates the formation of the Cu_2SnSe_3 phase. In addition, $SnSe_x$ is not detected at these initial stages when applying the Ge-doped precursor, in agreement with the lower loss of Sn detected by XRF. Thus, doping the bronze-based precursor with germanium promotes the incorporation of Sn into the Cu_2SnSe_3 phase instead of formation of the volatile $SnSe_x$ phase, which reduces the Sn loss by evaporation and, in turn, produces a higher Sn availability that can react to Cu and Se to form more Cu_2SnSe_3. Similarly to the above, the formation of CTZSe starts from 450 °C when applying the Ge-doped precursor, although, in this case, the relative intensity of the CZTSe absorber peaks with respect to the peaks of ZnSe and CuSe secondary phases is higher at the intermediate process stages (450 °C, 500 °C, and 550 °C). However, despite the accelerated formation of the Cu_2SnSe_3 phase promoted by the Ge-doped precursor, it can be observed that, at the end of the annealing process, the CZTSe absorber presents a similarly high crystalline quality regardless of the germanium doping. In fact, the Ge-doped precursor produces a higher relative intensity of the ZnSe secondary phase at the surface of the final absorber, in agreement with the higher [Zn]/[Sn] ratio detected by XRF.

It is well-known that Raman spectroscopy provides information from the surface and sub-surface of the absorber limited by the penetration depth of the excitation wavelengths; in consequence, XRD was applied to analyze the phase formation in the bulk of the absorbers. Figure 9 shows the X-ray diffractograms of the samples produced from Ge-free and Ge-doped bronze-based precursors at the different stages of the synthesis process in a selected range where relevant peaks were detected (full range can be observed in Supplementary Figure 11). The main difference between both precursors is observed at 400 °C, where the Ge-free precursor shows the formation of Cu-Se phases that are not detected when applying the Ge-doped precursor, in agreement with the surface analysis performed above by Raman spectroscopy. At the same temperature, the Ge-doped precursor produces a sample with SnSe and Cu_5Zn_8 in its bulk, some phases that are already detected in the previous synthesis stage for both precursors but that are not detected for the Ge-free one at 400 °C. Consistent with the Raman spectroscopy results, the XRD data are corroborated by XRF measurements, which reveal a greater loss of Sn and a resulting Cu excess during the early stages of processing for the Ge-free precursor. This issue is mitigated by the incorporation of germanium in the precursor. Despite this difference at 400 °C, both Ge-free and Ge-doped precursors produce the same phases at the other synthesis temperatures, including the last process stage. In both cases, the Cu_6Sn_5 phase is detected only in the precursor, so the bronze phase is completely reacted even at the lowest analyzed annealing temperature, which indicates that it plays a role in the CZTSe formation that confirms the interest in having Cu-Sn in the precursor target to allow a higher control of the CZTSe formation process. As it is

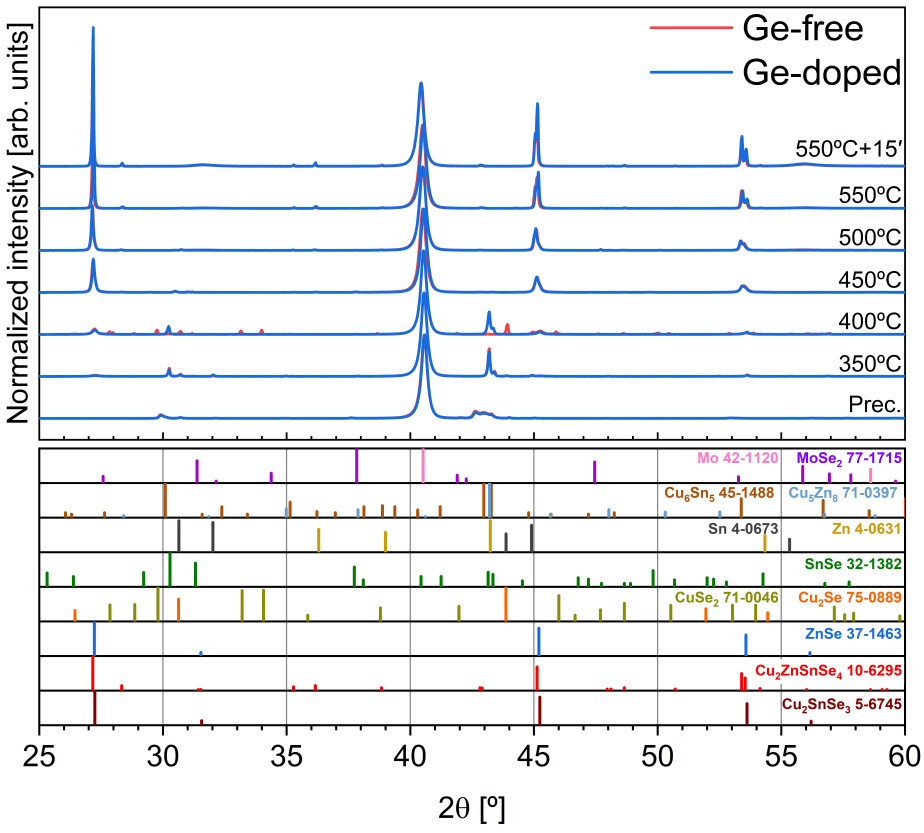

Figure 9. X-ray diffractograms of samples produced at different stages of a one-step annealing process from Ge-free and Ge-doped bronze-based precursors. All diffractograms are normalized to Mo reflection peak at 40.5°. Under the measured diffractograms, the patterns of different phases observed during the formation are listed and the numbers behind each phase correspond to reference patterns in ICDD database. ICDD: International centre for diffraction data.

well-known, most of the XRD reflections of ZnSe and Cu_2SnSe_3 phases are overlapped, so discriminating the presence of these two phases in the absorber bulk by this technique is difficult. In any case, both precursors produce an increase with the annealing temperature of the relative intensity of the 27.2° reflection, which also contains contributions from the CZTSe phase, which is coherent with the results obtained by Raman spectroscopy. Finally, the relative intensity of the 36.1° reflection indicates the formation of CZTSe in the bulk of the absorber at 450 °C regardless of the Ge doping, and its relative concentration increases with the annealing temperature, in agreement with the Raman spectroscopy results. Thus, XRD shows a different formation of binary compounds in the bulk of the absorber at the initial stages of the annealing process depending on the Ge doping, but this difference is not translated into any notable difference in the final absorber.

In summary, both Ge-free and Ge-doped bronze-based precursors promote the formation of the Cu_2SnSe_3 ternary phase at early stages of the annealing process, which reduces the intermediate phases during the CZTSe formation pathway and, in consequence, minimizes the absorber surface defects and maximizes the device efficiency[19-21]. While this formation of the Cu_2SnSe_3 phase had already been reported in the case of Ge-free bronze-based precursors[28,29], no reported studies existed analyzing the impact of germanium doping on bronze-based precursors, which is a critical strategy in the case of the elemental metallic stack precursor to achieve a ternary-based reaction pathway to form CZTSe and to achieve high-efficiency devices[23,31]. The results of this work reveal that doping the bronze-based precursor with germanium

accelerates the Cu_2SnSe_3 formation due to a lower loss of Sn at the initial process stages, but the final CZTSe absorber presents similar structural properties regardless of the germanium doping. From a formation pathway perspective, the use of germanium can be omitted when utilizing bronze-based precursors, offering a significant advantage over elemental metallic stack precursors.

Effect on the optoelectronic parameters

Solar cell devices were produced from the CZTSe absorbers synthesized at the last stage of the annealing process shown in Supplementary Figure 1B from both Ge-free and Ge-doped bronze-based precursors. The optoelectronic characteristics of the resulting devices are shown in Figure 10, which shows that doping the bronze-based precursor with germanium improves the V_{OC} of the solar cells, but reduces their J_{SC} and FF with respect to the Ge-free samples. In consequence, the efficiency of the produced devices is similar regardless of the Ge doping, as can be observed in Figure 10D. Moreover, analysis of the dispersion of the optoelectronic parameters between the solar cells of the two analyzed samples shows a high increase of the CV value in the Ge-doped samples. This can be attributed to the non-uniform deposition of the nanometric Ge layer, which assumes the presence of an additional synthesis process step that requires optimization and precise control. So, the application of germanium doping to bronze-based precursors can be avoided without decreasing the final performance of the CZTSe-based solar cells, which represents another advantage of this precursor with respect to the elemental metallic stack precursor.

CONCLUSIONS

This work analyzed the impact of applying bronze-based precursors to produce CZTSe-based solar cells as compared to applying elemental metallic stack precursors to determine which is the optimum precursor for the sequential fabrication of such solar cells based on physical deposition methods. First, SEM, EDX, and XRD revealed that the bronze-based precursor presents improved morphology, higher lateral compositional micro-homogeneity, and a higher presence of binary alloys than the elemental metallic stack precursor. Then, SEM observation showed that the positive characteristics of the bronze-based precursor produce CZTSe absorbers with an improved thickness homogeneity and an improved morphology of the rear interface, which presents a reduction of the presence of voids and, therefore, a higher contact area between the absorber and the back contact. This improved homogeneity of the thickness and the rear interface morphology allows an increase in the J_{SC} of the CZTSe-based solar cells. In addition, Raman spectroscopy detected an improved crystalline quality at the absorber surface when the bronze-based precursor is applied, as well as a possible improved structural micro-homogeneity at the absorber surface. These structural improvements could explain the low V_{OC} deficit achieved in the literature when applying bronze-based precursors[27,33]. Finally, it was demonstrated that the germanium doping that is required in the case of the elemental metallic stack precursor can be avoided when applying the bronze-based precursor without altering the CZTSe formation pathways and without compromising the device performance.

In conclusion, this work sheds light on the impact of bronze-based precursors on CZTSe absorbers, explaining the high and reproducible efficiencies of the solar cells produced from this type of precursor reported in the literature[26,27]. Additionally, presenting for the first time a direct comparison between the elemental metallic stack precursor and the bronze-based precursor to produce CZTSe-based solar cells, this work demonstrates that the bronze-based precursor provides several advantages when producing CZTSe-based solar cells by physical deposition methods, since it improves different properties of the CZTSe absorbers with respect to the elemental metallic stack precursor, and it offers a reproducible and simpler fabrication process that will help to scale-up the CZTSe technology to the industrial level, in addition to reduce the consumption of material, energy and time, leading to an economical and environmental benefit.

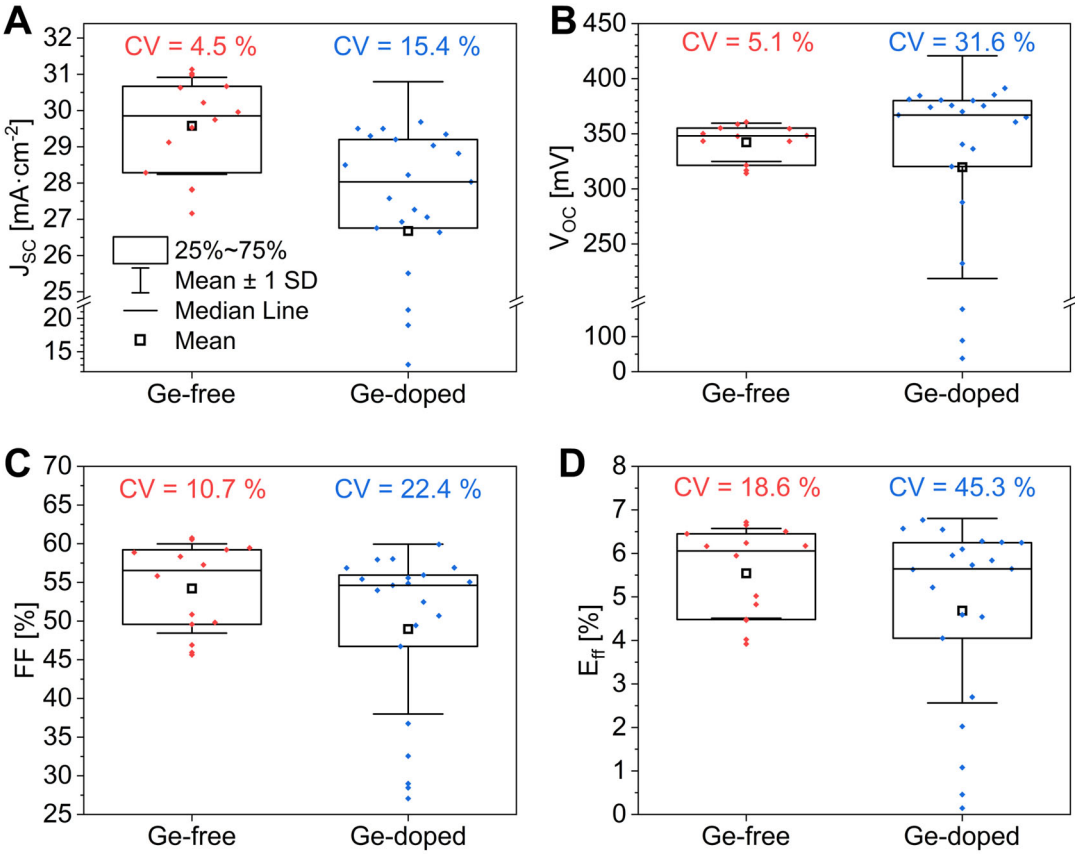

Figure 10. (A) Short-circuit current density, (B) open-circuit voltage, (C) fill factor, and (D) energy conversion efficiency of CZTSe-based solar cells produced from Ge-free and Ge-doped bronze-based precursors. The coefficient of variation is indicated for each parameter and sample. CZTSe: $Cu_2ZnSnSe_4$.

Finally, this work also indicates possible objectives for future studies regarding CZTSe-based solar cells. Considering the improved wettability of the bronze-based precursor on the Mo-coated substrate, future studies should aim to optimize the back contact. Then, since the surface of the CZTSe absorber is flatter and more regular when applying bronze-based precursors, an optimization of the buffer and window layers is also possible for future studies; e.g., the possibility of reducing the thickness of the CdS buffer layer can be considered. The advancements demonstrated in this work using bronze-based precursors, along with the potential future improvements, pave the way for bringing CZTSe-based technology closer to the transition to industrial-like scale production.

DECLARATIONS

Authors' contributions

Idea conception: Izquierdo-Roca, V.

Writing - original draft: Fonoll-Rubio, R.

Writing - editing: Fonoll-Rubio, R.; Vidal-Fuentes, P.; Guc M.

Materials characterization: Fonoll-Rubio, R.; González-Castillo, J. R.; Andrade-Arvizu, J.; Alcobé, X.; Izquierdo-Roca, V.

Samples synthesis: González-Castillo, J. R.; Andrade-Arvizu, J.

Funding acquisition, supervision: Pérez-Rodríguez, A.; Guc, M.; Izquierdo-Roca, V.

All authors participated in the data analysis and result discussions and commented on the manuscript.

Availability of data and materials

The data that support the findings of this study are available from the corresponding author upon reasonable request.

Financial support and sponsorship

This study was partially funded by the European Union H2020 Framework Programme under Grant Agreement no. 952982 (Custom-Art) and by the MCIN/AEI/10.13039/501100011033, FEDER, EU through the SCALING Project (PID2022-138434OB-C52). Authors from IREC belong to the MNT-Solar Consolidated Research Group of the "Generalitat de Catalunya" (ref. 2021 SGR 01286) and are grateful to the European Regional Development Funds (ERDF, FEDER Programa Competitivitat de Catalunya 2007-2013). M.G. acknowledges the financial support from MCIN/AEI/10.13039/501100011033 and FSE+ within the Ramón y Cajal (RYC2022-035588-I) program. J. A.-A. acknowledges that this publication is part of the Juan de la Cierva (JDC2023-051452-I) grant, funded by MICIU/AEI/10.13039/501100011033 and FSE+.

Conflicts of interest

All authors declared that there are no conflicts of interest.

Ethical approval and consent to participate

Not applicable.

Consent for publication

Not applicable.

REFERENCES

1. Kinnaird, J. A.; Nex, P. A. Critical raw materials . In: Yakovleva, N.; Nickless, E.; editors. *Routledge handbook of the extractive industries and sustainable development*. London: Routledge; 2022. pp. 13-33. DOI
2. Lee, T. D.; Ebong, A. U. A review of thin film solar cell technologies and challenges. *Renew. Sustain. Energy. Rev.* **2017**, *70*, 1286-97. DOI
3. Candelise, C.; Winskel, M.; Gross, R. Implications for CdTe and CIGS technologies production costs of indium and tellurium scarcity. *Prog. Photovolt. Res. Appl.* **2012**, *20*, 816-31. DOI
4. Wang, A.; Chang, N. L.; Sun, K.; et al. Analysis of manufacturing cost and market niches for Cu_2ZnSnS_4 (CZTS) solar cells. *Sustain. Energy. Fuels.* **2021**, *5*, 1044-58. DOI
5. Li, J.; Sun, K.; Yuan, X.; Huang, J.; Green, M. A.; Hao, X. Emergence of flexible kesterite solar cells: progress and perspectives. *npj. Flex. Electron.* **2023**, *7*, 16. DOI
6. Tripathi, S.; Maurya, S.; Kumar, B.; Dwivedi, D. K. Comparative analysis of CZTS/CZTSe/CZTSSe absorber layer for solar cell applications. In: 2020 International Conference on Electrical and Electronics Engineering (ICE3); 2020 Feb 14-15; Gorakhpur, India. IEEE; 2020. pp. 588-91. DOI
7. Andrade-Arvizu, J.; Izquierdo-Roca, V.; Becerril-Romero, I.; et al. Is it possible to develop complex S-Se graded band gap profiles in kesterite-based solar cells? *ACS. Appl. Mater. Interfaces.* **2019**, *11*, 32945-56. DOI
8. Andrade-arvizu, J.; Fonoll-rubio, R.; Sánchez, Y.; et al. Rear band gap grading strategies on Sn-Ge-alloyed kesterite solar cells. *ACS. Appl. Energy. Mater.* **2020**, *3*, 10362-75. DOI
9. Andrade-Arvizu, J.; Rubio, R. F.; Izquierdo-Roca, V.; et al. Controlling the anionic ratio and gradient in kesterite technology. *ACS. Appl. Mater. Interfaces.* **2022**, *14*, 1177-86. DOI PubMed PMC
10. Mathews, I.; Kantareddy, S. N.; Buonassisi, T.; Peters, I. M. Technology and market perspective for indoor photovoltaic cells. *Joule* **2019**, *3*, 1415-26. DOI
11. Ghosh, A. Potential of building integrated and attached/applied photovoltaic (BIPV/BAPV) for adaptive less energy-hungry building's skin: a comprehensive review. *J. Clean. Prod.* **2020**, *276*, 123343. DOI
12. Dinesh, H.; Pearce, J. M. The potential of agrivoltaic systems. *Renew. Sustain. Energy. Rev.* **2016**, *54*, 299-308. DOI

13. Green, M. A.; Dunlop, E. D.; Yoshita, M.; et al. Solar cell efficiency tables (Version 63). *Prog. Photovolt. Res. Appl.* **2024**, *32*, 3-13. Available from: https://onlinelibrary.wiley.com/doi/full/10.1002/pip.3750. [Last accessed on 26 Mar 2025]
14. Grenet, L.; Suzon, M. A. A.; Emieux, F.; Roux, F. Analysis of failure modes in kesterite solar cells. *ACS. Appl. Energy. Mater.* **2018**, *1*, 2103-13. DOI
15. Fonoll-rubio, R.; Andrade-arvizu, J.; Blanco-portals, J.; et al. Insights into interface and bulk defects in a high efficiency kesterite-based device. *Energy. Environ. Sci.* **2021**, *14*, 507-23. DOI
16. Schorr, S.; Gurieva, G.; Guc, M.; et al. Point defects, compositional fluctuations, and secondary phases in non-stoichiometric kesterites. *J. Phys. Energy.* **2020**, *2*, 012002. DOI
17. Li, J.; Huang, J.; Ma, F.; et al. Unveiling microscopic carrier loss mechanisms in 12% efficient $Cu_2ZnSnSe_4$ solar cells. *Nat. Energy.* **2022**, *7*, 754-64. DOI
18. Giraldo, S.; Jehl, Z.; Placidi, M.; Izquierdo-Roca, V.; Pérez-Rodríguez, A.; Saucedo, E. Progress and perspectives of thin film kesterite photovoltaic technology: a critical review. *Adv. Mater.* **2019**, *31*, 1806692. DOI PubMed
19. Zhou, J.; Xu, X.; Wu, H.; et al. Control of the phase evolution of kesterite by tuning of the selenium partial pressure for solar cells with 13.8% certified efficiency. *Nat. Energy.* **2023**, *8*, 526-35. DOI
20. Gong, Y.; Zhang, Y.; Zhu, Q.; et al. Identifying the origin of the V_{oc} deficit of kesterite solar cells from the two grain growth mechanisms induced by Sn^{2+} and Sn^{4+} precursors in DMSO solution. *Energy. Environ. Sci.* **2021**, *14*, 2369-80. DOI
21. Gong, Y.; Zhang, Y.; Jedlicka, E.; et al. Sn^{4+} precursor enables 12.4% efficient kesterite solar cell from DMSO solution with open circuit voltage deficit below 0.30 V. *Sci. China. Mater.* **2021**, *64*, 52-60. DOI
22. Ratz, T.; Brammertz, G.; Caballero, R.; et al. Physical routes for the synthesis of kesterite. *J. Phys. Energy.* **2019**, *1*, 042003. DOI
23. Giraldo, S.; Saucedo, E.; Neuschitzer, M.; et al. How small amounts of Ge modify the formation pathways and crystallization of kesterites. *Energy. Environ. Sci.* **2018**, *11*, 582-93. DOI
24. Hernández-martínez, A.; Placidi, M.; Arqués, L.; et al. Insights into the formation pathways of $Cu_2ZnSnSe_4$ using rapid thermal processes. *ACS. Appl. Energy. Mater.* **2018**, *1*, 1981-9. DOI
25. Giraldo, S.; Kim, S.; Andrade-arvizu, J. A.; et al. Study and optimization of alternative MBE-deposited metallic precursors for highly efficient kesterite CZTSe:Ge solar cells. *Prog. Photovolt. Res. Appl.* **2019**, *27*, 779-88. DOI
26. Taskesen, T.; Steininger, V.; Chen, W.; et al. Resilient and reproducible processing for CZTSe solar cells in the range of 10%. *Prog. Photovolt. Res. Appl.* **2018**, *26*, 1003-6. DOI
27. Taskesen, T.; Neerken, J.; Schoneberg, J.; et al. Device characteristics of an 11.4% CZTSe solar cell fabricated from sputtered precursors. *Adv. Energy. Mater.* **2018**, *8*, 1703295. DOI
28. Pareek, D.; Taskesen, T.; Márquez, J. A.; et al. Reaction pathway for efficient $Cu_2ZnSnSe_4$ solar cells from alloyed Cu-Sn Precursor via a Cu-rich selenization stage. *Solar. RRL.* **2020**, *4*, 2000124. DOI
29. Taskesen, T.; Pareek, D.; Nowak, D.; et al. Potential of CZTSe solar cells fabricated by an alloy-based processing strategy. *Z. Naturforsch. A.* **2019**, *74*, 673-82. DOI
30. González-castillo, J.; Vigil-galán, O.; Rodríguez, E.; Jiménez-olarte, D.; Leal, J. Cu_6Sn_5 binary phase as a precursor material of the CZTSe compound: optimization of the synthesis process, physical properties and its performance as an absorbing material in a solar cell. *Mater. Scie. Semicond. Process.* **2021**, *134*, 106016. DOI
31. Giraldo, S.; Neuschitzer, M.; Thersleff, T.; et al. Large efficiency improvement in $Cu_2ZnSnSe_4$ solar cells by introducing a superficial Ge nanolayer. *Adv. Energy. Mater.* **2015**, *5*, 1501070. DOI
32. Fairbrother, A.; Fourdrinier, L.; Fontané, X.; et al. Precursor stack ordering effects in $Cu_2ZnSnSe_4$ thin films prepared by rapid thermal processing. *J. Phys. Chem. C.* **2014**, *118*, 17291-8. DOI
33. Nowak, D.; Taskesen, T.; Pareek, D.; Pfeiffelmann, T.; Mikolajczak, U.; Gütay, L. Tuning of precursor composition and formation pathway of kesterite absorbers using an in-process composition shift: a path toward higher efficiencies? *Solar. RRL.* **2021**, *5*, 2100237. DOI
34. Nowak, D.; Atlan, F.; Pareek, D.; et al. Influence of the precursor composition on the resulting absorber properties and defect concentration in $Cu_2ZnSnSe_4$ absorbers. *Sol. Energy. Mater. Sol. Cells.* **2023**, *256*, 112342. DOI
35. Delbos, S. Këwhile terite thin films for photovoltaics : a review. *EPJ. Photovolt.* **2012**, *3*, 35004. DOI
36. Márquez, J.; Neuschitzer, M.; Dimitrievska, M.; et al. Systematic compositional changes and their influence on lattice and optoelectronic properties of $Cu_2ZnSnSe_4$ kesterite solar cells. *Sol. Energy. Mater. Sol. Cells.* **2016**, *144*, 579-85. DOI
37. Heriche, H.; Rouabah, Z.; Bouarissa, N. New ultra thin CIGS structure solar cells using SCAPS simulation program. *Int. J. Hydrogen. Energy.* **2017**, *42*, 9524-32. DOI
38. Leonard, E.; Arzel, L.; Tomassini, M.; Zabierowski, P.; Marrón, D. F.; Barreau, N. $Cu(In,Ga)Se_2$ absorber thinning and the homo-interface model: influence of Mo back contact and 3-stage process on device characteristics. *J. Appl. Phys.* **2014**, *116*, 074512. DOI
39. Jehl, Z.; Erfurth, F.; Naghavi, N.; et al. Thinning of CIGS solar cells: part II: cell characterizations. *Thin. Solid. Films.* **2011**, *519*, 7212-5. DOI
40. Cheon, K. B.; Hwang, S. K.; Seo, S. W.; Park, J. H.; Park, M. A.; Kim, J. Y. Roughness-controlled $Cu_2ZnSn(S,Se)_4$ thin-film solar cells with reduced charge recombination. *ACS. Appl. Mater. Interfaces.* **2019**, *11*, 24088-95. DOI
41. Scragg, J. J.; Dale, P. J.; Colombara, D.; Peter, L. M. Thermodynamic aspects of the synthesis of thin-film materials for solar cells. *Chemphyschem* **2012**, *13*, 3035-46. DOI PubMed
42. López-marino, S.; Placidi, M.; Pérez-tomás, A.; et al. Inhibiting the absorber/Mo-back contact decomposition reaction in $Cu_2ZnSnSe_4$

solar cells: the role of a ZnO intermediate nanolayer. *J. Mater. Chem. A.* **2013**, *1*, 8338. DOI

43. Karade, V.; Lokhande, A.; Babar, P.; et al. Insights into kesterite's back contact interface: a status review. *Sol. Energy. Mater. Sol. Cells.* **2019**, *200*, 109911. DOI
44. Dimitrievska, M.; Oliva, F.; Guc, M.; et al. Defect characterisation in $Cu_2ZnSnSe_4$ kesterites *via* resonance Raman spectroscopy and the impact on optoelectronic solar cell properties. *J. Mater. Chem. A.* **2019**, *7*, 13293-304. DOI
45. Weber, A.; Krauth, H.; Perlt, S.; et al. Multi-stage evaporation of Cu_2ZnSnS_4 thin films. *Thin. Solid. Films.* **2009**, *517*, 2524-6. DOI
46. Stanchik, A.; Gremenok, V.; Juskenas, R.; et al. Effects of selenization time and temperature on the growth of $Cu_2ZnSnSe_4$ thin films on a metal substrate for flexible solar cells. *Solar. Energy.* **2019**, *178*, 142-9. DOI
47. Redinger, A.; Berg, D. M.; Dale, P. J.; Siebentritt, S. The consequences of kesterite equilibria for efficient solar cells. *J. Am. Chem. Soc.* **2011**, *133*, 3320-3. DOI
48. Guo, T.; Yu, Z.; Liu, L.; Zhao, Y.; Zhang, Y. Effect of substrate and selenization temperature on the properties of RF sputtered CZTSe layer. *Vacuum* **2017**, *145*, 217-24. DOI